Journal of The
Electrochemical Society

FUEL CELLS, ELECTROLYZERS, AND ENERGY CONVERSION • OPEN ACCESS

Continuous Graded Catalyst Layers for PEM Fuel Cells with Improved Humidity Range Tolerance

To cite this article: Marc Ayoub *et al* 2024 *J. Electrochem. Soc.* **171** 114503

Journal of The Electrochemical Society, 2024 **171** 114503

Continuous Graded Catalyst Layers for PEM Fuel Cells with Improved Humidity Range Tolerance

Marc Ayoub,[1,2] Anna T. S. Freiberg,[1,2,*] Thomas Böhm,[1] Andreas Körner,[1,2] Andreas Hutzler,[1] Simon Thiele,[1,2] and Matthew Brodt[1,,z]**

[1]*Helmholtz-Institute Erlangen-Nürnberg for Renewable Energy (IET-2), Forschungszentrum Jülich, 91058 Erlangen, Germany*
[2]*Department of Chemical and Biological Engineering, Friedrich-Alexander-Universität Erlangen-Nürnberg, 91058 Erlangen, Germany*

Grading electrodes is a promising approach to reduce ohmic and mass transport-related voltage losses in proton exchange membrane fuel cells. In graded electrodes, the ionomer and/or catalyst are spatially non-uniformly distributed to optimize performance over a wide operating range. In this study, through-plane ionomer gradients were fabricated with a simple wet-layer deposition technique that can readily be adapted in a roll-to-roll process. The presence of ionomer gradients was verified using scanning transmission electron microscopy and the profiles were found to be continuous despite using only two coating steps. Single cell tests revealed that the gradients outperform conventional electrodes and maintain the optimal performance for different relative humidities. These improvements were traced back to enhanced mass transport and protonic conduction properties identified by detailed electrochemical analysis. This manufacturing approach for electrodes offers an accessible toolbox to produce versatile and specialized multi-layered catalyst layers for different applications.
 [DOI: 10.1149/1945-7111/ad8d81]

Manuscript submitted August 2, 2024; revised manuscript received October 23, 2024. Published November 11, 2024.

Supplementary material for this article is available online

Low-temperature proton exchange membrane fuel cells (LT-PEMFCs) are a critical research focus and development field for the energy transition of the 21st century. The usage of hydrogen in PEMFCs potentially bridges the gap between energy storage and end-user applications because of its high gravimetric energy density.[1,2] End-user applications include the automotive sector as an example. A series of car models based on H_2-PEMFC systems are already commercially available.[3] However, high system costs, expensive raw materials, insufficient durability, and a small optimum operation window still impede mass commercialization.[4,5] To tackle these challenges, many researchers have been focusing on developing and optimizing catalyst layers, using low equivalent weight ionomers and alloy-based catalysts, and optimizing the design and properties of the catalyst layer itself.[6–10]

The focus of catalyst layer research in hydrogen PEMFCs has been on optimizing the cathode electrode. In the cathode, protons from the hydrogen oxidation reaction (HOR) arrive from the anode and react with oxygen and electrons via the oxygen reduction reaction (ORR) to form water. The ORR is typically six orders of magnitudes slower than the HOR.[11–13] As a result, higher Pt-catalyst loadings are utilized, making catalytic activity and utilization central financial aspects.

One optimization approach to tackle the challenges associated with the cathode is the improvement of the spatial distribution of the chemical constituents of the electrode by manufacturing graded catalyst layers (GCLs). In GCLs, the grading directions can be through-plane (TP), perpendicular to the membrane-electrode interface, or in-plane (IP), parallel to the membrane's interface.[6,7] Literature reports different GCL types, like ionomer, and catalyst concentration gradients.[14–17] Ionomer gradients are particularly interesting when considering the dynamic changes in the RH of an operating fuel cell. A few studies have already experimentally touched on the benefits of TP ionomer gradients.[14,18–21] For example, Xie et al.[18] and Kim et al.[19] saw improved performance with increasing ionomer contents towards the membrane. However, the polarization curve measurements were performed only in almost fully humidified conditions. Chen et al.[20] tested increasing TP ionomer gradients towards the membrane at 80% and 20% RH. However, only one non-graded ionomer-to-carbon ratio was used for comparison, and different operating conditions are expected to require different optimum ionomer contents. These studies were the first steps in illustrating the importance of TP ionomer gradients. However, there is still ample space for further investigations before exploiting the potential benefits at an industrially relevant level.

For example, it is unknown if industrially relevant materials can be used for the ionomer gradients. It is also not clear if fast coating techniques can be utilized, which are valuable for an economy of scale effect. So far, high equivalent weight (EW $\geqslant$ 1000 g·mol^{-1}) ionomers like Nafion^{TM} were mostly studied; low EW ones have not yet become a focus.[18–20] Although a recent study reports the application of a novel fluorine-free ionomer with EW $\sim$ 333 g·mol^{-1} for graded catalyst layers, these materials are still in an early research stage, and more research on the novel fluorine-free ionomers is required.[21] Furthermore, spray coating was utilized as a coating technique in most prior studies, which typically is an order of magnitude slower than wet-layer deposition techniques like slot die coating, and it has narrow viscosity ranges for the inks.[22]

Here, the manufacturing of ionomer GCLs using a low-EW perfluorinated sulfonic acid ionomer with doctor blading as a fast and scalable coating technique is reported. In a simple two-step coating procedure, continuous GCLs were produced that exhibit superior tolerance to changes in the RH compared to non-graded references. The gradients were visualized and confirmed using scanning transmission electron microscopy with energy-dispersive X-ray spectroscopy (STEM-EDXS) on ultramicrotome-cut sections. The observed performance improvements were further analyzed and attributed to enhanced proton conduction in the catalyst layers and lower mass transport resistances. This scalable method for gradient production paves the way for accessible fine-tuning of membrane electrode assemblies in industrial applications.

Experimental

Ink preparation.—A 20 wt% short side chain (SSC) 3 M^{TM} ionomer dispersion (EW $\sim$ 800 g·mol^{-1}) was prepared in a 60 wt%

*Electrochemical Society Student Member.
**Electrochemical Society Member.
[z]E-mail: ma.brodt@fz-juelich.de

n-propanol and 40 wt% water mixture. The mixture was prepared by first adding alcohol to the ionomer, allowing the ionomer to swell for one hour, followed by adding water. The dispersion was then placed on a heating plate set at ∼120 °C with a magnetic stirring bar at 250 ∼ 300 rpm and dispersed over three days. The internal temperature corresponded to ∼70 °C. All CLs were prepared with this ionomer dispersion, including the anode CLs.

A commercial Vulcan-based Pt/C catalyst (TEC10V30E, ∼30 wt % Pt/C, Tanaka) was used to prepare all inks, including the anode CLs. The inks were prepared by first adding water to the catalyst, followed by n-propanol (water:n-propanol weight ratio, 2:3), and then the ionomer dispersion. The total solid weight content of the inks, including the catalyst and dry ionomer, was 10 wt%, and the solvent content was 40 wt% water with the balance n-propanol. The inks were prepared by roller mixing for 18–22 h. The non-graded catalyst layers' ionomer-to-carbon ratios (I/C) were 0.65, 0.80, and 1.00. For all samples, an anode CL with an I/C of 0.65 was used.

Catalyst layer and CCM fabrication.—Catalyst layers were doctor-bladed on virgin PTFE decal foils having a thickness of ∼50 μm. A coating table with active heating and a suction option was used for the manufacturing (Coatmaster 510, Erichsen). The coating table was set at 60 °C, and the decal foils were placed on top while the vacuum suction option was switched on. The inks were pipetted on the decal sheets and coated with a doctor blade (Proceq ZUA 2000.100), ensuring film widths of 100 mm. The homogeneous CLs with I/C ratios of 0.65, also used for anodes, were coated at a gap size of 275 μm. The homogeneous cathode catalyst layers with I/C ratios of 0.80 and 1.00 were coated with gap sizes of 280 μm and 290 μm, respectively with the intention of achieving similar Platinum loadings. The average cathode catalyst layer thicknesses are ∼17, 13, and 12 μm for the I/C ratios of 0.65, 0.80, and 1.00 (Fig. S1 and Table S1). Coatings were produced using a viscous ionomer dispersion for the ink, applied on virgin white PTFE sheets and no visible cracks could be seen when the samples were held up to the light. To produce the graded CL, first, a coating via doctor-blading of ink with an I/C ratio of 0.65 was done at a gap size of 160 μm and left to dry on the 60 °C heated plate. Then, a second coating directly on top of the first using ink with an I/C ratio of 1.00 at a gap size of 170 μm was applied. The loadings obtained from the coatings were similar, $0.160 \pm 0.010\ mg_{Pt} \cdot cm^{-2}$ per coating and the catalyst layer thickness was ∼15.0 μm (Fig. S1 and Table S1). All decal-coated substrates were dried in a convective oven at 120 °C for 1 h. The overall Pt-loading was $0.310 \pm 0.030\ mg_{Pt} \cdot cm^{-2}$ for all cathodes making an intercomparison reasonable, and $0.245 \pm 0.105\ mg_{Pt} \cdot cm^{-2}$ for the anodes ensuring that the anode is not the limiting electrode.

Once dried, the sheets were cut into 5 cm^2 electrodes ($2.23 \cdot 2.23\ cm^2$) and hot-pressed onto $\sim 5 \cdot 5\ cm^2$ ($25\ cm^2$) GORE-SELECT® Membrane M775.15; (thickness 15.5 μm, W.L. Gore Associates) forming the CCMs. For this, a Kapton® foil was placed onto a $5 \cdot 5\ cm^2$ Pacopad™ (Pacopad #5500, Pacothane Technologies) sheet for an even pressure distribution.[23] Afterward, the anode was placed on the Kapton® sheet, followed by the membrane and the cathode. Finally, another Kapton® sheet was placed on the cathode, followed by another Pacopad™ sheet. Then, the CCM was hot-pressed (Lab Line P 200S, Collin Lab Pilot Solutions) in three steps. First, the sample was preconditioned for 60 s at 120 °C and 0.5 MPa to desiccate the electrodes and membrane. Then, the temperature was ramped up to 155 °C in 150 s. Finally, the pressure was increased to 1.2 MPa and held for 240 s. Catalyst loadings were determined gravimetrically by weighing the decal foils before and after hot-pressing.

Electrochemical polarization characterization.—Three MEAs for each I/C ratio were tested using an 850e FC test system (Scribner Associates Inc.) with a VSP-300 or VMP-300 potentiostat (BioLogic). The same hydrophobic gas diffusion layers (GDLs), including a microporous layer, were used for the anode and cathode (5 cm^2 H14CX483, Freudenberg). Glass-fiber-reinforced PTFE gaskets were used to compress the GDLs to 27 ± 2% of the original thickness, and a torque of 5 N·m was applied to assemble the cell. The cell fixture was a commercial 5 cm^2 cell from Scribner with graphite flow fields with a single-channel serpentine flow path (1 mm land width, channel width, and depth). Cell tests were started with a short test at 80 °C under fully humidified conditions by performing a linear sweep voltammetry (LSV) measurement with $0.20\ l \cdot min^{-1}$ N_2 and $0.20\ l \cdot min^{-1}$ H_2 with a scan rate of $2\ mV \cdot s^{-1}$ starting from roughly 0.10 V up to 0.6 V at ambient pressure.[24–26]

If no short was detected, the cell was conditioned according to Murthy et al.[27] by voltage cycling 4–10 times between 0.6 V and 0.3 V until no further considerable improvement in current density could be observed at the respective voltages. Each voltage was held for 20 min, and two minutes open circuit voltage periods were used between the cycles. The conditioning step was performed at $0.20\ l \cdot min^{-1}$ H_2, $0.75\ l \cdot min^{-1}$ synthetic air, 50 kPa gauge pressure on both sides, and 94% RH (dew point = 78.5 °C). Once conditioned, a polarization curve measurement was conducted at this operating point using a combination of potentiostatic ($V_{start} = 1.00$ V, $\Delta V = 0.05$ V, $V_{end} = 0.75$ V) steps in the low current density region (<0.2 A cm^{-2}) and galvanostatic steps for the rest of the polarization curve ($i_{start} = 0.20\ A \cdot cm^{-2}$, $i_{max} = 2.20\ A \cdot cm^{-2}$). The hold time of each step was 2 min. The last 30 s were averaged to represent the polarization response. At each polarization step, electrochemical impedance spectra in the frequency range of 100 kHz to at least 0.4 Hz were recorded after the hold, with 10 points per decade and five averaged measurements per frequency, and with excitation perturbations of 2 mV for the potentiostatic steps, and 10% of the total current for the galvanostatic steps. The highest frequency used for analysis was limited to 30 kHz, as noise from the setup significantly increased at higher frequencies.

Proton sheet resistance, electrode capacitance, and ECSA determination.—The cathode was purged with nitrogen after each polarization analysis, followed by an impedance measurement for proton sheet conduction evaluation under atmospheric pressure and a flow rate of $0.20\ l \cdot min^{-1}$ N_2 for the cathode and $0.20\ l \cdot min^{-1}$ H_2 for the anode.[28–31] The voltage was set at 0.2 V under blocking conditions and was sinusoidally alternated with an amplitude of 10 mV from 100 kHz to 0.2 Hz with 10 points per decade and five averaged measurements per frequency. To obtain an estimated proton sheet resistance, the impedance spectra under blocking conditions were fitted with an equivalent circuit consisting of an inductor, a resistance, and a transmission line model (TLM) with infinite charge transfer resistance in series.[30] The fit was done using the built-in ZFit function in the EC-Lab software, with the built-in "Randomize+Simplex" method. We use the symbol $\bar{\sigma}$ for the conductivities obtained from this analysis (that inherently assumes a homogeneous conductivity throughout the CLs in the through-plane direction) to differentiate them from the spatially resolved conductivities that are explained later.

Cyclic voltammetry measurements were performed by scanning the voltage from 0.03 V to 0.6 V with a $100\ mV \cdot s^{-1}$ scan rate at all investigated humidity conditions under N_2 atmosphere at the cathode (0 flow). This data was used to estimate the volumetric double-layer capacitance used later for the model developed by Reshetenko and Kulikovsky[29] for non-uniform protonic conduction in catalyst layers.

At the end of the measurement protocol, including the different humidity conditions, cyclic voltammograms at 40 °C and 100% RH were recorded for all CCMs to estimate the electrochemical surface area (ECSA). The N_2 flow rate was set to 0 to avoid removal of the hydrogen that diffused through the membrane to the cathode by a convective gas flow, which would result in different concentration profiles and a distorted hydrogen underpotential region.[32,33] The ECSA ($m^2 \cdot g_{Pt}^{-1}$) was estimated based on the charge q^{HUPD} ($C \cdot m^{-2}$) observed in the HUPD region and the platinum loading of the electrode L_{Pt} ($g_{Pt} \cdot m^{-2}$) assuming a theoretical adsorption charge on a smooth polycrystalline platinum surface of $\bar{q}_{pcPt}^{H-ads} = 210\ \mu C \cdot cm_{Pt}^{-2}$ according to Eq. 1.[25,26,34]

$$\mathrm{ECSA} = \frac{q^{HUPD}}{\bar{q}_{pcPt}^{H-ads} \cdot L_{Pt}} \quad [1]$$

The charge was determined by integrating the hydrogen underpotential desorption area within a potential range from 0.05 V to 0.4 V.

Catalyst layer mass transport resistance analysis.—Limiting current experiments were done under atmospheric pressure in the presence of 3 vol%, 3.5 vol%, 4 vol%, and 5 vol% oxygen in nitrogen gas with a total flow rate of 0.95 l·min^{-1}. To achieve those dry oxygen contents, synthetic air and nitrogen were mixed at the respective ratios using a gas mixing interface (Scribner Associates Inc.).

The voltages were stepped in potentiostatic mode from 0.5 V to 0.1 V ($\Delta V = 0.08$ V), with a hold time of at least 60 s at every step. The last 30 s of the last step were averaged to get the current response i_{lim}. From this, the mass transport resistance $R_{T,O2}$ was determined accordingly using Eq. 2.[35]

$$i_{\mathrm{lim}} = \frac{4 \cdot F}{R_{\mathrm{T,O_2}}} \cdot \frac{p_{\mathrm{abs}} - p_{\mathrm{H_2O}}}{R \cdot T} \cdot \quad x_{\mathrm{O_2,dry}} \quad [2]$$

F is the Faraday constant (96485 A·s·mol^{-1}), $x_{O2,dry}$ is the dry mole fraction of O_2 in the gas stream, R is the universal gas constant (8.3145 J·mol^{-1} ·K^{-1}), T is the cell temperature i_{lim} is the measured limitting current, p_{abs} is the absolute gas pressure and p_{H_2O} the partial pressure of water.

All electrochemical tests described before were done at three different humidification conditions: 94% RH symmetric, 30% RH symmetric, and 15% RH symmetric. A polarization curve was also obtained with a dry cathode and the anode at 15% RH. The four different CCM types with varying cathode ionomer content (I/C = 0.65, 0.80, 1.00, and graded 0.65//1.0) were tested.

Non-uniform protonic conduction in catalyst layers.—For homogeneous proton conduction throughout the thickness of a CL, a simple transmission line model can be used to quantify the proton sheet resistance. However, for CLs exhibiting an inhomogeneous ionomer distribution in through–plane direction (either intentionally formed or naturally occurring during electrode drying), the requirements to apply a simple transmission line model are not met, and the corresponding impedance response does not show a 45° line under blocking conditions in the mid-frequency range. Reshetenko and Kulikovsky[29] developed an analytical impedance model for non-uniform distributions of ionomer throughout the CL, which was applied under blocking conditions in this study.[29] With the characteristic parameter β in the model, the uniformity of the proton conductivity can be estimated, and the proton conductivity distribution across the CL thickness $\sigma_p(x)$ can be described using:

$$\sigma_{\mathrm{p}}(x) = \sigma_0 \cdot \mathrm{e}^{(-\beta \cdot x)} \quad [3]$$

Here, x denotes the normalized catalyst layer thickness.[29] The proton conductivity at the CL-membrane interface ($x = 0$) is σ_0 and the local proton conductivity at the CL-GDL interface can be calculated at $x = 1$. A value of $\beta = 0$ represents a homogeneous ionomer distribution whereas positive β values indicate a decreasing proton conductivity toward the CL-GDL interface.. Further discussion is provided in section S3 of the SI.

STEM-EDXS analysis.—After testing, one MEA per I/C ratio was embedded in epoxy resin (Araldite 502) and prepared for transmission electron microscopy by ultramicrotomy. Standard cross-sectional SEM-EDXS does not provide a sufficient resolution to identify electrode composition gradients, which is why high-resolution STEM-EDXs was performed. Ultrathin sections (nominal thickness of 100–150 nm) were cut using a Diatome ultra 45° diamond knife on an RMC Boeckeler PowerTome (PowerTome), and the sections were collected on lacey carbon-coated copper grids. Then, high-angle annular dark field STEM (HAADF-STEM) and STEM-EDXS were performed with a Talos F200i (Thermo Fisher Scientific). Imaging was performed at an acceleration voltage of 80 kV to mitigate beam damage to the ionomer.

SEM analysis.—After testing, every MEA was embedded in epoxy resin to cross-sectionally determine the electrode thicknesses by SEM imaging (Fig. S1). EpoThin resin and hardener (Buehler) were used for the embedding. The MEAs were first placed between two PTFE sheets in embedding cups before hardening overnight at room temperature. Once hardened, the samples were ground with SiC sanding papers (Struers GmbH), successively from 500 to 4000-grain sizes using a LaboForce 100 polishing machine (Struers GmbH). Afterwards, the samples were polished with an MD-Mol polishing plate using a diamond solution, DiaPro Mol B 3 μm (Struers GmbH). The embedded samples were then gold-sputtered to improve their conductivity (Cressington 108 manual) and placed with conductive copper tape (Plano GmbH) under a scanning electron microscope (Tescan Vega 3). The measurements were done at 20 kV using a secondary electron detector with a working distance of 5 mm. The thicknesses given in Fig. S1 are the average thickness over a view field of 200 μm.

Results and Discussion

STEM-EDXS.—The presence of gradients was verified using STEM-EDX spectrum imaging. This approach offers the required resolution and elemental contrast to identify through-plane gradients in catalyst layers. Figure 1 shows the variation of the fluorine and platinum signals from the spectrum imaging for electrodes with an I/C ratio of 0.65 (a), 0.80 (b), 1.00 (c), and the graded CL with I/C ratios of 0.65/1.0 (d). The first column shows the HAADF images of all samples, followed by the spectrum images of the CLs with respect to the fluorine signal of the ionomer (orange) and the platinum signal of the catalyst particles (blue). In the fourth column, the average EDX intensities over the width of the mappings are shown.

As illustrated in Figs. 1a and 1b, the I/C ratios of 0.65 and 0.80 have constant fluorine and platinum signals across the catalyst layers, indicating the presence of majorly homogeneous ionomer and catalyst distribution.

For an I/C ratio of 1.00, a minor increase of the F signal in the CL toward the CL/membrane interface can be seen (Fig. 1c). Influencing parameters for the natural gradient can include the water-to-alcohol ratio in the ink and the drying procedure.[36–39] At such high I/C ratios, the natural gradient could also be intensified due to more free ionomer not directly bound to the catalyst during the drying process.

The intentionally graded sample shown in Fig. 1d, however, shows a clear and more pronounced gradient in the catalyst layer. Notably, the ionomer gradient shows a continuous increase in the ionomer content from the GDL towards the membrane despite being manufactured with only two coating steps. Without intermixing, the two coatings should result in a distinct I/C step between the two layers. However, this step was not visible, which can be explained by the partial dissolution of the first deposited layer during the second coating. Consequently, the layers can partially mix at their interface, resulting in a more continuous gradient in ionomer content between the two layers.

Additional STEM-EDXS spectrum images can be found in Fig. S2. In there similar trends can be seen for the samples. To confidently verify the presence of the ionomer gradient, four additional measurements were included in Fig. S2. One has to note that the thicknesses measured in Fig. S1 are statistically more relevant than the thicknesses from the STEM-EDXS analysis, since the cross-sections for the STEM-EDXS have a very limited field of view. Nevertheless, the measured thicknesses are in line with the ones of Fig. S1 (Measured electrodes are noted in Fig. S1). A comparison of the spatially resolved fluorine to platinum ratio

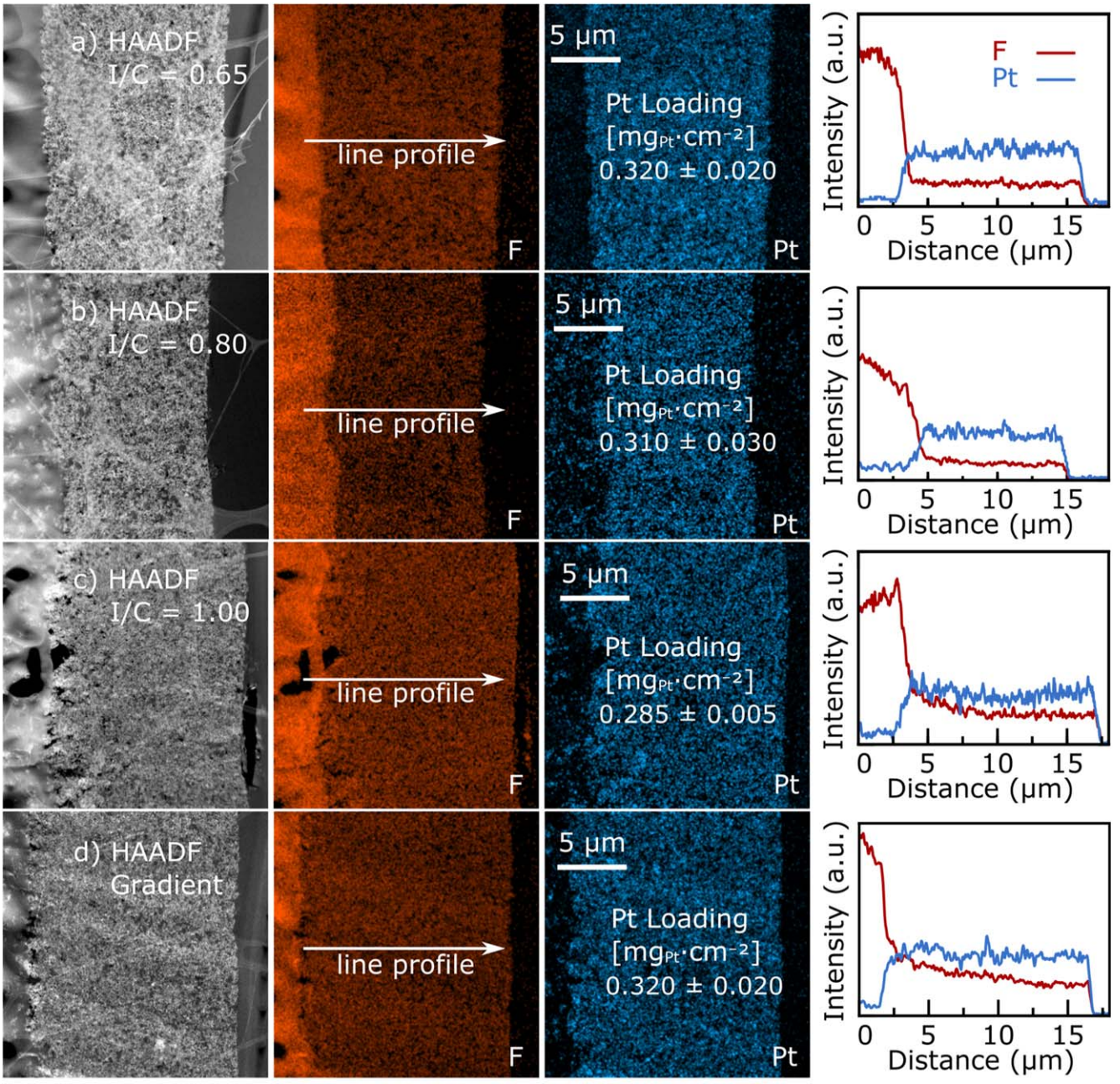

Figure 1. Electron microscopic evaluation of the catalyst layers. The image panels show HAADF-STEM images (left panel) as well as EDX spectrum images of fluorine (second panel) and platinum (third panel). The graphs depict the intensity line profiles integrated over the whole image, showing the F intensity signal in orange and the Pt intensity signal in blue; (a) Displays an I/C ratio of 0.65, (b) an I/C ratio of 0.80, (c) an I/C ratio of 1.00, and (d) the graded cathode catalyst layer with I/C ratios of 0.65//1.00. The images show catalyst layers from the membrane-facing side (left in the micrographs) to the GDL-facing side (right in the micrographs). The slightly brighter spider-web-like regions in the HAADF-STEM images depict the underlying lacey carbon layer of the copper sample grids.

obtained by STEM-EDXS with the proton conductivity profile of the different cathode CLs is discussed later (see Fig. 5). Table S1 further shows that the I/C ratio of 0.65 has the highest void volume fractions at different relative humidities, whereas the I/C ratio of 1.00 has the lowest. The gradient shows values in between, similar to the I/C ratio of 0.80. Along with the observed gradient, the cross-sectional SEM images, and the void volume fractions, a porosity gradient increasing towards the GDL interface is also obtained, consistent with previous findings.[18]

Electrochemical Characterization

Polarization curves were recorded at symmetric RHs of 94%, 30%, 15%, and 15% RH at the anode and a completely dry cathode (0//15% RH) for the different I/C ratios and the gradient sample. Averaged polarization curves based on three samples for each I/C ratio and the corresponding power densities can be seen in Fig. 2. The measurements show that the optimal I/C ratio of non-graded samples depends strongly on the RH, as expected.

At high humidification (94% RH, Fig. 2a), all samples behave very similarly at typical operating conditions above 0.6 V, with the only apparent difference being an earlier onset of mass transport limitation for the high I/C ratio of 1.00 distinguishable at around 0.5 V (yellow triangles). Upon decreasing the humidification to 30% (Fig. 2b) and 15% (Fig. 2c), the ohmic contribution from reduced proton conductivity led to significant performance loss for the sample with an I/C ratio of 0.65, at typical operating conditions around 0.6 V (black diamonds). For those operating conditions, the

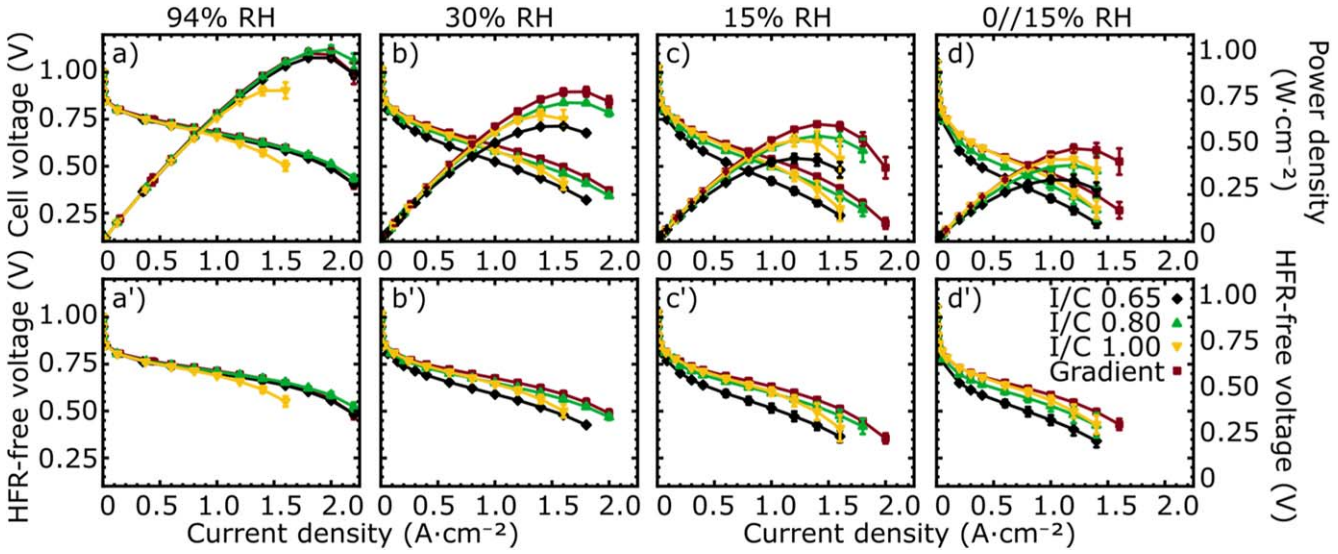

Figure 2. Average polarization curves and HFR-free curves, based on three samples per configuration with flow rates of 0.2 l·min^{-1} H_2 at the anode and 0.75 l·min^{-1} air at the cathode with 50 kPa gauge backpressure at 80 °C and (a) RH 94% at the cathode and anode, (b) RH 30% at the cathode and anode, c) RH 15% at the cathode and anode, (d) RH 15% at the anode and a dry cathode (0//15% RH). (a′), (b′), (c′). and (d′) are the HFR-Free polarization curves, and error bars depict the standard deviation of the three measurements per sample.

best-performing MEA with a homogeneous I/C ratio in the cathode is the sample set using an I/C of 0.80 (green triangles). The mass transport limitation, visible around 0.5 V and below, of the MEA with an I/C of 1.00 at the cathode is still decreasing the overall performance compared to the sample with an I/C ratio of 0.80. When switching to a completely dry cathode feed with low humidification on the anode (Fig. 2d), the sample with an I/C ratio of 0.80 starts to show increased ohmic limitations at typical operating conditions above 0.6 V, similar to the MEA with an I/C ratio of 0.65. This led to a performance worse than the sample with the highest I/C ratio of 1.00 above 0.6 V. At lower voltages in the mass transport region ∼0.5 V, similar end currents are achieved due to the higher mass transport resistance for the I/C ratio of 1.00.

Notably, the ionomer-graded catalyst layer (red squares) achieved similar or better performance compared with the optimal non-graded samples at all investigated RH levels. Due to the low ionomer content close to the GDL interface, the mass transport resistance visible around 0.5 V and below, is similar to the sample with the lowest I/C ratio of 0.65 (see Fig. 2a). On the other hand, the high I/C ratio close to the membrane led to similar ohmic behavior as the I/C ratio of 1.00 at 0.6 V and above, which in turn still allowed decent performance at dry operating conditions (see Fig. 2d).

This behavior is more clearly represented in Figs. 3a and 3b, where the power densities are shown normalized to the highest power density among the different I/C ratios; the normalization was done once at peak power density and once at 0.6 V (interpolated). This representation shows that the non-graded samples have an optimal RH operation regime, either at low or high RH, and lose performance when leaving this ideal operation window. The graded catalyst layer, however, shows a high relative power density at all RHs. Thus, the data of the graded catalyst layer indicates a wider humidity operation window compared to the non-graded MEAs.

We performed additional electrochemical analysis to determine the reasons for the different RH tolerances. The ECSAs of all samples were similar, with values of roughly 80 $m^2 \cdot g_{Pt}^{-1}$ (Table S2 and Fig. S3).

Limiting current experiments were conducted to gain insight into the mass transport properties of the samples (Fig. S4). The mass transport resistances for the I/C ratio of 1.00 showed the highest values, irrespective of the RH. The gradient and the I/C ratios of 0.65 showed lower and similar values, indicating better mass transport properties (Table I). Hence, although the gradient sample partially consists of an I/C of 1.00, it still shows better mass transport properties.

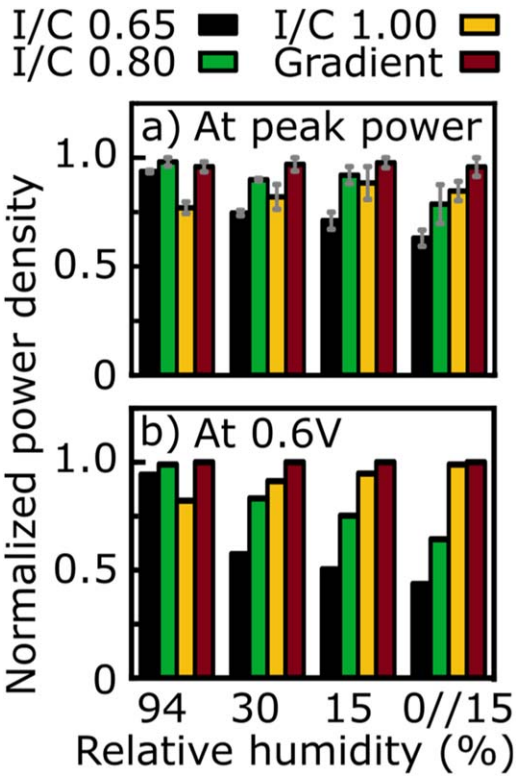

Figure 3. Normalized power density from polarization curve measurements at (a) peak power density and (b) power density at 0.6 V. The normalization was done based on the highest power density achieved at the different tested relative humidities among the different I/C ratios. The normalization in (b) at 0.6 V was done via linear interpolation and, therefore, doesn't include error bars. The error bars in (a) depict the standard deviation of the three measured samples per configuration.

Electrochemical impedance spectroscopy under blocking conditions was measured to quantitatively compare the proton conductivity in CLs. The angles of the samples were screened using a quick

Table I. Mass transport resistances based on limiting current experiments at different RHs. The data was recorded at atmospheric pressure with 0.2 l·min^{-1} H_2 in the anode and 0.95 l·min^{-1} N_2 in the cathode with 3%, 3.5%, 4%, and 5% of O_2. Mean and standard deviations are from the individual mass transport resistance values calculated at the different O_2 concentrations for one sample of each I/C ratio.

	I/C 0.65	I/C 0.80	I/C 1.00	Gradient
R (s·cm^{-1}) at RH 94%	0.619 ± 0.001	0.633 ± 0.003	0.789 ± 0.003	0.630 ± 0.001
R (s·cm^{-1}) at RH 30%	1.083 ± 0.013	1.112 ± 0.016	1.326 ± 0.023	1.081 ± 0.017
R (s·cm^{-1}) at RH 15%	1.487 ± 0.018	1.788 ± 0.027	1.948 ± 0.017	1.557 ± 0.012

linear fit in the mid-frequency region (Section S3). It is commonly agreed that a homogeneous catalyst layer results in a 45° line in the Nyquist representation.[29,40] From the fits, it is observed that the graded sample shows angles considerably larger than 45°, Fig. 4a. The non-graded samples had smaller values, decreasing with lower I/Cs. The observed angle shifts among the non-graded samples are probably caused by the formation of small natural gradients during the drying process, as discussed in the STEM-EDXS analysis. Notably, the effect of inhomogeneous ionomer distributions in PEMFC electrodes has already been identified as a possible reason for this apparent shift in angle, including a fading transition to the capacitive behavior at low frequencies.[41,42] Thus, this data aligns with the ionomer gradient trend observed in the STEM-EDXS data and suggests that the shape and/or angle from the Nyquist plots of the impedance spectra in the mid-frequency regions could be used as a quick screening tool to check the homogeneity of proton conductivity inside a catalyst layer.

For electrodes with homogeneous ionomer distribution across the thickness of the CL, a reasonable impedance model is a transmission line model with infinite charge transfer resistance and one value for the ionic resistance in each infinitely small segment throughout the CL.[30,31] This common data analysis was executed for all samples in this study, neglecting contributions from the anode CL. A representative fit is shown in Fig. S5. The values for the proton sheet resistances resulting from these fits are shown in Fig. 4b. These were converted into conductivities and normalized to the electrode thicknesses in Fig. 4c. Overall, the conductivity increases with increasing I/C ratio. The gradient has a better conductivity than the middle I/C ratio of 0.80 and is close to the conductivity of the MEA with an I/C ratio of 1.00.

The use of the aforementioned transmission line model is limited to homogeneous ionomer distributions in the CL. While the fit reflects the data reasonably well for the homogeneous samples, an intrinsic assumption error is made when applying this model to the graded CL. The usage of one constant value for the local proton resistance in the CL constrains the impedance response to follow a 45° line in the Nyquist representation in the mid-frequency region. This clearly deviates from the real scenario. A more sophisticated model must be used to account for the inhomogeneous proton conductivity in the CLs. One possibility is to use a transmission line model with a finite number of coupling capacitors, allowing each ionic resistor in the equivalent circuit to be different. The quality of such a fit would largely depend on the size of the transmission line model, the amount of data available, and the choice of boundary and coupling parameters (i.e., when analyzing data obtained at different humidities). A more elegant way is the use of an analytical model with a shape function describing the local proton transport resistance through the CL. An analytical solution for a shape function following an exponential decay was developed by Reshetenko and Kulikovsky,[29] as given in Eq. 3.

Based on the STEM-EDXS results showing a gradual change in fluorine signal through the CL thickness (see Fig. 1d), we employed this model to represent our data (see section S3 in the SI). Also, the nominally homogeneous I/C samples were fitted with this model for comparison. A β value of 0 corresponds to a uniform conduction profile, whereas higher values result in steeper profiles and account for the deviation from the 45° angle (section S3).

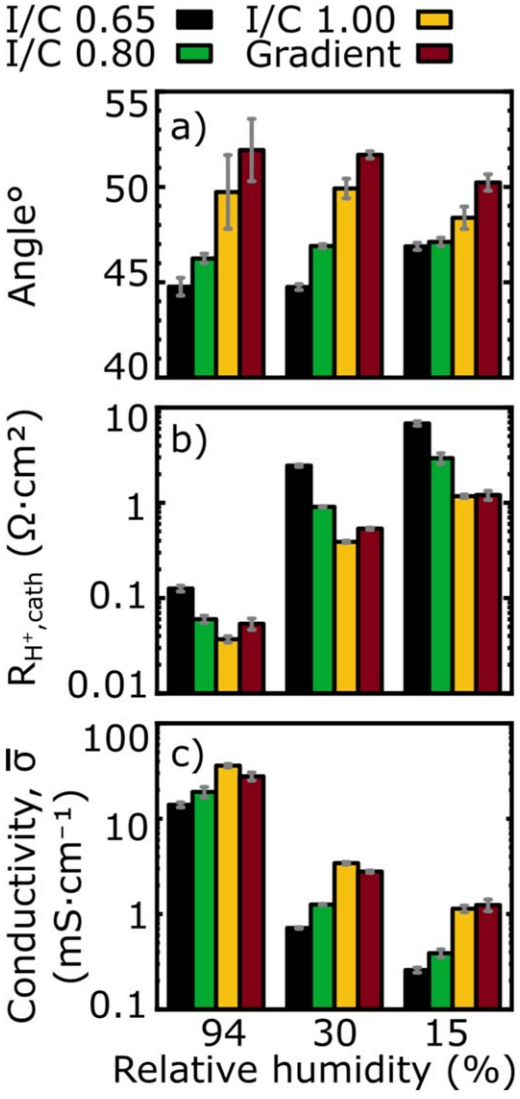

Figure 4. Evaluation of impedance measurements under blocking conditions. (a) Angles fitted in the linear region of the Nyquist plot. See section S3 for detailed information regarding measurement and evaluation. (b) Proton sheet resistance under different RHs assuming homogeneous catalyst layers and isotropic conditions. (c) Conductivity values for proton transport under different RHs assuming homogeneous catalyst layers and isotropic conditions.

Initial guesses for the conductivity values, σ_0, were taken from the transmission line model results (Fig. 4c) and iteratively changed using a global optimization algorithm in Python, differential_evolution, from the scipy.optimize module, and a huber_loss error function (see section S3). The resulting conductivity profiles in the catalyst layers were then plotted (dashed lines in Fig. 5). The observed trends for the conductivity profiles of the proton transport

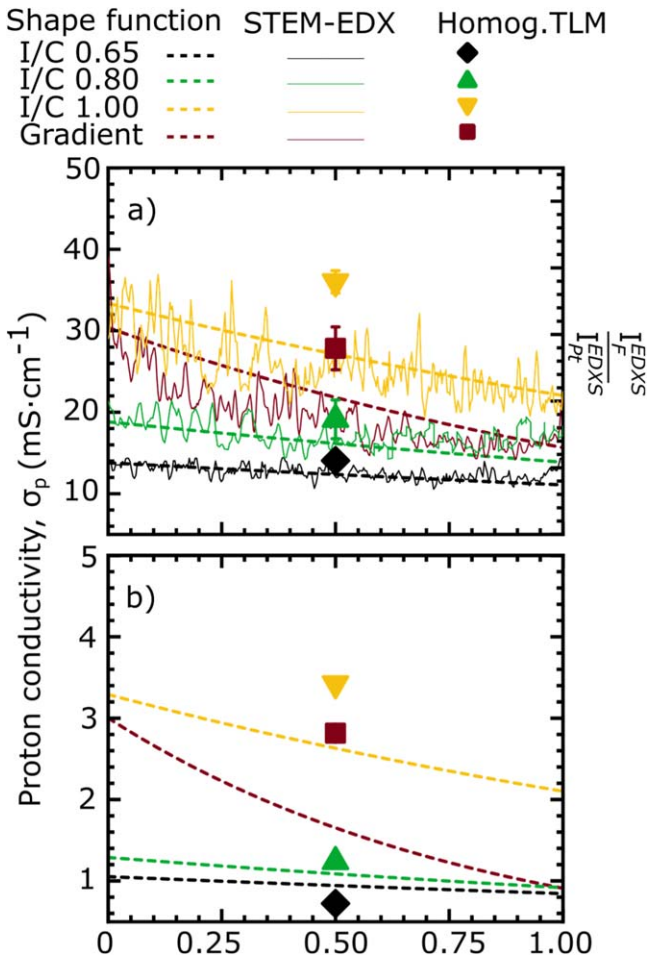

Figure 5. Conduction profiles for proton transport in the catalyst layer from membrane interface (position 0) to the GDL interface (position 1.00) assuming an exponentially decaying function for the conductivity as in[29] at (a) RH 94%, and (b) RH 30%. In (a) the ratios of the fluorine to platinum signals from the EDX spectra are plotted on the second *y*-axis. The conductivities from the homogeneous TLM are plotted at a normalized position of 0.5.

are in line with the average transmission line model results (denoted as open symbols at $x = 0.5$). Notably, the conduction profile in the catalyst layer becomes more non-uniform as the I/C ratio increases, and the graded sample shows the steepest profile. The variation in the conductivity profiles goes hand in hand with the spectrum images. The higher the variation of the ionomer in the catalyst layer, the steeper the observed conduction profile. For direct comparison, the intensity ratios of the fluorine to platinum signals from the STEM-EDXS analysis are added to Fig. 5a as thin lines (right-hand scale). A direct link between the conductivity profiles and the ionomer-to-platinum ratio is difficult to obtain in the form of a simple equation. However, a general agreement of the microscopic results to the proton transport profiles can be observed.

Conclusions

In this study, continuous graded catalyst layers were successfully fabricated using a low-equivalent-weight ionomer and a two-step doctor-blading coating method, a scalable technique. The presence of the ionomer gradient was verified using STEM-EDXS measurements on ultramicrotome cross-sections of the MEAs. The electrochemical characterization of the MEAs with graded cathode catalyst layer and homogeneous catalyst layers of different I/C ratios showed increased tolerance of the graded MEA to variations in the relative humidity of the gas feeds. The graded cathode MEA exhibited optimized proton and mass transport properties that enable a wider operational window for the fuel cell. Mass transport properties were quantified using limiting current experiments. The experiments revealed that the graded catalyst layer has better mass transport properties compared to the I/C ratio of 1.00, explaining its superior performance at high relative humidity. From a homogeneous impedance transmission line model, comparable proton conductivity values were measured under blocking conditions for the graded MEA and an I/C ratio of 1.00. A similar trend was observed when a transient impedance model was used for the analysis. By employing an exponentially decaying function to describe the conduction profile for proton transport, the graded catalyst layer exhibited more pronounced variations in through-plane conductivity, as anticipated. The conductivity increased towards the membrane interface, reaching values close to those of an I/C of 1.00 despite a lower total ionomer content in the catalyst layer. Similar profile shapes were also observed when the fluorine-to-platinum ratios were plotted from the STEM-EDXS analysis on the same graph. Given the accessibility and scalability of the manufacturing approach, this study paves the way for industrial applications and further optimization toward efficient and robust catalyst layers.

Acknowledgments

We gratefully acknowledge the financial support provided in the frame of the POREForm project funded by the German Federal Ministry for Economic Affairs and Energy (BMWK; funding number 03ETB027A). Andreas Körner and Andreas Hutzler also thank the German Ministry of Education and Research (BMBF) for financial support within the project H_2Giga—StacIE (03HY103H). We express our gratitude to 3 M™ for providing the ionomer for this study.

ORCID

Marc Ayoub https://orcid.org/0009-0001-9977-254X
Anna T. S. Freiberg https://orcid.org/0000-0002-7885-7632
Thomas Böhm https://orcid.org/0000-0003-2036-2159
Andreas Körner https://orcid.org/0000-0001-8679-8743
Andreas Hutzler https://orcid.org/0000-0001-5484-707X
Simon Thiele https://orcid.org/0000-0002-4248-2752
Matthew Brodt https://orcid.org/0000-0002-6895-9889

References

1. United Nations Framework Convention on Climate Change; The Paris Agreement; UNFCCC, Accessed October 19, Published October 19, 2015. https://unfccc.int/sites/default/files/english_paris_agreement.pdf.
2. European Sustainable Development Network (ESDN). The European Green Deal and the 2030 Agenda for Sustainable Development: An Analysis of their Relationships; (2020), Accessed October 19, 2023, https://www.esdn.eu/fileadmin/ESDN_Reports/ESDN_Report_2_2020.pdf.
3. H2.LIVE. Fuel Cell Electric Vehicle - H2.LIVE. (Accessed October 19, 2023), https://h2.live/en/fcev/.
4. Multi-Annual Work Plan (MAWP) J. U. Clean Hydrogen Joint Undertaking, (2014), https://www.clean-hydrogen.europa.eu/document/download/29a7bd1b-5c19-4202-8fd2-dbfad804c6bf_en.
5. U.S. Department of Energy, U.S. DRIVE Fuel Cell Technical Team Roadmap, (November 2017), https://www.energy.gov/eere/vehicles/articles/us-drive-fuel-cell-technical-team-roadmap.
6. S. Ebrahimi, B. Ghorbani, and K. Vijayaraghavan, "Optimization of catalyst distribution along PEMFC channel through a numerical two-phase model and genetic algorithm." *Renewable Energy*, **113**, 846 (2017).
7. L. Xing et al., "Membrane electrode assemblies for PEM fuel cells: a review of functional graded design and optimization." *Energy*, **177**, 445 (2019).
8. M. Breitwieser, M. Klingele, S. Vierrath, R. Zengerle, and S. Thiele, "Tailoring the membrane-electrode interface in PEM fuel cells: a review and perspective on novel engineering approaches." *Adv. Energy Mater.*, **8**, 1701257 (2018).
9. E4tech. Materia. The Fuel Cell Industry Review 2021. 2021. Published July 2021 (2021), Environmental Resource Management (ERM) https://www.erm.com/globalassets/documents/fuel-cell-industry-review/thefuelcellindustryreview2021.pdf.
10. A. J. Appleby, "Electrocatalysis and fuel cells." *Catalysis Reviews*, **4**, 221 (1971).
11. B. Emonts, L. Blum, T. Grube, W. Lehnert, J. Mergel, M. Müller, and R. Peters, *Fuel Cell Technology and Applications; Part 1: Pt. 1* (Wiley, New York) (2003), Reprinted.
12. A. Damjanovic and V. Brusic, "Electrode kinetics of oxygen reduction on oxide-free platinum electrodes." *Electrochim. Acta*, **12**, 615 (1967).

13. D. Gidaspow, "Handbook of fuel cell technology, Carl Berger, Editor, Prentice-Hall, Englewood Cliffs, N. J. (1968). 607 pages. $18.50." *AlChE J.*, **15**, 3 (1969).
14. Q. Wang et al., "Functionally graded cathode catalyst layers for polymer electrolyte fuel cells." *J. Electrochem. Soc.*, **151**, A950 (2004).
15. R. Lin, H. Wang, and Y. Zhu, "Optimizing the structural design of cathode catalyst layer for PEM fuel cells for improving mass-specific power density." *Energy*, **221**, 119909 (2021).
16. C-W. Roh, J. Choi, and H. Lee, "Hydrophilic-hydrophobic dual catalyst layers for proton exchange membrane fuel cells under low humidity." *Electrochem. Commun.*, **97**, 105 (2018).
17. Y. Qiu, H. Zhang, H. Zhong, and F. Zhang, "A novel cathode structure with double catalyst layers and low Pt loading for proton exchange membrane fuel cells." *Int. J. Hydrogen Energy*, **38**, 5836 (2013).
18. Z. Xie et al., "Functionally graded cathode catalyst layers for polymer electrolyte fuel cells." *J. Electrochem. Soc.*, **152**, A1171 (2005).
19. K-H. Kim et al., "Effect of Nafion® gradient in dual catalyst layer on proton exchange membrane fuel cell performance." *Int. J. Hydrogen Energy*, **33**, 2783 (2008).
20. G-Y. Chen et al., "Gradient design of Pt/C ratio and Nafion content in cathode catalyst layer of PEMFCs." *Int. J. Hydrogen Energy*, **42**, 29960 (2017).
21. H. Nguyen, D. Sultanova, P. A. Heizmann, S. Vierrath, and M. Breitwieser, "Improving the efficiency of fully hydrocarbon-based proton-exchange membrane fuel cells by ionomer content gradients in cathode catalyst layers." *Mater. Adv.*, **3**, 8460 (2022).
22. M. Bodner et al., "Enabling industrial production of electrodes by use of slot-die coating for HT-PEM fuel cells." *Int. J. Hydrog Energy*, **44**, 12793 (2019).
23. F. Arslan et al., "Performance of quaternized polybenzimidazole-cross-linked poly (vinylbenzyl chloride) membranes in HT-PEMFCs." *ACS Appl. Mater. Interfaces*, **13**, 56584 (2021).
24. P. Zihrul, "Untersuchungen zur Aktivität und Stabilitätvon Membran-Elektroden-Einheitenfür PEM-Brennstoffzellen." *M.Sc*, TU Munich (2018), https://mediatum.ub.tum.de/1449745.
25. J. Zhang, H. Zhang, J. Wu, and J. Zhang, *PEM Fuel Cell Testing and Diagnosis* (Elsevier, Amsterdam) (2013).
26. H. H. Wang, X-Z. Yuan, and H. Li, *PEM Fuel Cell Durability Handbook* (CRC Press/Taylor & Francis, Boca Raton) 4, 81 (2012).
27. M. Murthy, N. T. Sisofo, and C. A. Baczkowki, *Method and device to improve operation of a fuel cell*, Canada, CA2595222A1 (2005).
28. D. Gerteisen, "Impact of inhomogeneous catalyst layer properties on impedance spectra of polymer electrolyte membrane fuel cells." *J. Electrochem. Soc.*, **162**, F1431 (2015).
29. T. Reshetenko and A. Kulikovsky, "Impedance spectroscopy study of the PEM fuel cell cathode with nonuniform nafion loading." *J. Electrochem. Soc.*, **164**, E3016 (2017).
30. Y. Liu et al., "Proton conduction and oxygen reduction kinetics in PEM fuel cell cathodes: effects of ionomer-to-carbon ratio and relative humidity." *J. Electrochem. Soc.*, **156**, B970 (2009).
31. K. C. Neyerlin, W. Gu, J. Jorne, A. Clark, and H. A. Gasteiger, "Cathode catalyst utilization for the ORR in a PEMFC." *J. Electrochem. Soc.*, **154**, B279 (2007).
32. M. Edmundson and F. C. Busby, "Overcoming artifacts in cyclic voltammetry through the use of multiple scan rates and potential windows." *ECS Trans.*, **41**, 661 (2011).
33. H. A. Gasteiger, S. S. Kocha, F. Wagner, and R. N. Carter, "Artifacts in measuring electrode catalyst area of fuel cells through cyclic voltammetry." *Meet. Abstr.*, **MA2007-02**, 469 (2007).
34. In Situ PEM FC Electrochemical Surface Area and Catalyst Utilization Measurement Scribner Associates, (January 26, 2018), https://www.scribner.com/faq/1-in-situ-pem-fc-electrochemical-surface-area-and-catalyst-utilization-measurement/.
35. D. R. Baker, D. A. Caulk, K. C. Neyerlin, and M. W. Murphy, "Measurement of oxygen transport resistance in PEM fuel cells by limiting current methods." *J. Electrochem. Soc.*, **156**, B991 (2009).
36. C. M. Cardinal, Y. D. Jung, K. H. Ahn, and L. F. Francis, "Drying regime maps for particulate coatings." *AlChE J.*, **56**, 2769 (2010).
37. S. A. Mauger et al., "Influence of ink formulation and drying conditions on ionomer distribution in high-performance roll-to-roll-coated gas-diffusion electrodes." *Meet. Abstr.*, **MA2020-02**, 2218 (2020).
38. D. K. Makepeace et al., "Stratification in binary colloidal polymer films: experiment and simulations." *Soft Matter*, **13**, 6969 (2017).
39. T. van Cleve et al., "Dictating Pt-based electrocatalyst performance in polymer electrolyte fuel cells, from formulation to application." *ACS Appl. Mater. Interfaces*, **11**, 46953 (2019).
40. M. Eikerling and A. Kornyshev, "Electrochemical impedance of the cathode catalyst layer in polymer electrolyte fuel cells." *J. Electroanal. Chem.*, **475**, 107 (1999).
41. G. Li and P. G. Pickup, "Ionic conductivity of PEMFC electrodes." *J. Electrochem. Soc.*, **150**, C745 (2003).
42. M. C. Lefebvre, "Characterization of ionic conductivity profiles within proton exchange membrane fuel cell gas diffusion electrodes by impedance spectroscopy." *Electrochem. Solid-State Lett.*, **2**, 259 (1999).